Particle size recognition by deterministic approaches and deep neural networks using astigmatism particle tracking velocimetry (APTV)

Sebastian Sachs[1,*], Manuel Ratz[1], Patrick Mäder[2], Jörg König[1], Christian Cierpka[1]

1: Institute of Thermodynamics and Fluid Mechanics, Technische Universität Ilmenau, Germany
2: Group for Software Engineering for Safety-Critical Systems, Technische Universität Ilmenau, Germany
*Corresponding author: sebastian.sachs@tu-ilmenau.de

Keywords: APTV, size recognition, deep neural network, microfluidics

ABSTRACT

The systematic manipulation of components of multimodal particle solutions is a key for the design of modern industrial products and pharmaceuticals with highly customized properties. In order to optimize innovative particle separation devices on microfluidic scales, a particle size recognition with simultaneous volumetric position determination is essential. In the present study, the astigmatism particle tracking velocimetry (APTV) is extended by two deterministic approaches and a deep neural network (DNN) to include size classification of particles of multimodal size distribution. Without any adaptation of the existing measurement setup, a reliable classification of bimodal particle solutions in the size range of $1.14\,\mu m$ to $5.03\,\mu m$ is demonstrated with a precision of up to $99.8\,\%$. Concurrently, the high detection rate of the particles is quantified by a recall of $97.6\,\%$. In the second part of the study, the introduced algorithms are applied to multi-class problems and analyzed comparatively. The high precision of $99.3\,\%$ confirms the performance and applicability of the presented algorithms for particle size recognition of up to four particle species.

1. Introduction

The mixing and separation of microparticles with various sizes is of crucial importance for the optimization of pharmaceutical products, paints and coatings, as well as building materials such as cement (Sajeesh & Sen, 2014). Innovative processes based on microfluidic lab-on-a-chip devices have achieved major advances for the systematic manipulation of the composition of particle solutions. In order to evaluate the performance and further optimize these processes, a particle size recognition is essential. Commercial particle size analysis devices require the separate examination of samples obtained from outlets, while in-process size recognition often utilizes particles with different fluorescent dye in conjunction with multiple long-pass filters. To overcome these limitations, the present work aims at the simultaneous size recognition and position determination of suspended particles by analyzing defocused particle images obtained from astigmatism particle tracking velocimetry (APTV) measurements.

The APTV evolved as a reliable tool for three-dimensional, three component (3D3C) velocity measurements in microfluidic environments with limited optical access by integrating a cylindrical lens in the optical path to the camera (Cierpka et al., 2010). As this lens reduces the focal length along one axis of the camera sensor, while keeping the focal length constant along the other axis, captured particle images appear elliptically shaped. Based on the lengths of the semi-axes of the ellipses (a_x, a_y), the depth position (z) of monodisperse tracers is mapped by a calibration function, that is obtained from previously captured particles with known z-position (Cierpka et al., 2011). Due to the geometric dependency between the size of a particle and the size of its particle image (Rossi et al., 2012), a monomodal size distribution is commonly used for velocity measurements. However, by including particle size recognition algorithms in the evaluation of particle images, the depth position of particles with multimodal size distribution can be determined based on the assigned calibration function. In this way, precise APTV measurements are achievable throughout the entire measurement volume with only one fluorescent dye and one camera, even when a multimodal particle solution is used.

The size recognition is addressed by two techniques. First, deterministic approaches were developed to achieve the discrimination between various particle sizes by different particle image shapes (see section 3.1) or by the intensity of the particle images (see section 3.2). Second, a deep neural network (DNN) is trained for object detection of particles in the images. The DNN is capable not only of determining the in-plane coordinates (x, y) of the particles, but also of assigning the found particles to different classes of objects according to their size. In the work of König et al. (2020), DNNs performed robustly even when using bimodal particle mixtures, with deviations an order of magnitude smaller than those of the classical APTV evaluation. However, in their study no classification regarding the particle size was done. The performance of the proposed techniques is evaluated on real images captured in a laminar fluid flow using a bimodal particle mixture in section 4.1. By combining the images of different bimodal particle mixtures, a size classification into multiple classes is further investigated in section 4.2. Finally, the results are summarized and compared.

2. Experimental setup

To compare the performance of the different algorithms, images of spherical particles with monodisperse diameter distribution of $1.14\,\mu m$, $2.47\,\mu m$, $3.16\,\mu m$ and $5.03\,\mu m$ were acquired. The fluorescent polystyrene particles (PS-FluoRed, MicroParticles GmbH) were suspended in an aqueous glycerol solution (80/20 w/w deionized water/glycerol) to reduce sedimentation. The fluid was pumped through a microchannel made of polydimethylsiloxane (PDMS) with a rectangular cross-section (approx. $500 \times 185\,\mu m^2$) at a constant flow rate of $5\,\mu L/min$ using a syringe pump (neMESYS, cetoni GmbH). In order to calculate regression planes of the intensity distribution (see section 3.2) and to provide training data for the DNN (see section 3.3), APTV measurements were first performed with a monomodal particle solution. The size recognition was subsequently based

on measurements using particles of bimodal size distribution in a microchannel with three inlets. The two particle types of different sizes were fed individually through the outer inlets, while pure fluid was fed in the middle inlet to spatially separate the particle types across the channel width. In this way, the ground truth for particle size recognition was determined based on the particle positions along the channel width, while particle images of two different classes were contained in one image. The ratio between the outer and inner volume flow rates was 1.5:2:1.5.

The microchannel was positioned on top of an inverted microscope (Axio Observer 7, Zeiss GmbH) with a plan neofluar objective (M20x, NA = 0.4, Zeiss GmbH). A modulatable OPSL laser (tarm laser technologies tlt GmbH & Co.KG) was used to volumetrically illuminate the particles through the channel bottom composed of $128°$ YX LiNbO$_3$. This piezoelectric substrate is widely used for particle separation devices based on surface acoustic waves (Wu et al., 2019; Sachs et al., 2022). Since particle size recognition provides essential advantages for the optimization of those systems, the described experiment was designed close to the intended application. Due to the birefringence of the fluorescent light beam in the LiNbO$_3$ crystal, a linear polarization filter was inserted into the optical path to the camera. For detection, the reflected laser light was removed from the fluorescent light of the particles by a dichroic mirror (DMLP567T, Thorlabs Inc) and a long pass filter (FELH0550, Thorlabs Inc). In addition, a cylindrical lens was positioned approximately $40\,\mathrm{mm}$ in front of an sCMOS camera (imager sCMOS, LaVision GmbH, 16 bit, 2560×2160 pixel) to introduce astigmatism into the optical system. At each measurement position, 1000 double frame images were acquired with a frame rate of $10\,\mathrm{Hz}$. To cover the entire channel height, the measurement volume was traversed in 8 steps in depth direction with a step size of $\Delta z = 20\,\mu\mathrm{m}$. For further evaluation, the relative depth position z' of the particles in the respective measurement volume was used. Additional details about the measurement setup can be found in Sachs et al. (2022).

As part of the classical image evaluation, the acquired images were preprocessed using a background subtraction and smoothed by a Gaussian filter with a kernel size of 5×5 pixel. Particle images were then segmented by a global threshold in the intensity profile. The in-plane positions and the lengths of the semi-axes of the elliptical particle images $(a_\mathrm{x}, a_\mathrm{y})$ were determined by one-dimensional Gaussian fits in the x- and y-direction with subpixel accuracy (Cierpka et al., 2012). When the DNN was used for image evaluation, the in-plane positions of the particles were determined during the object detection based on the center of the proposed bounding boxes (see section 3.3). The depth position of the particles was assigned based on $(a_\mathrm{x}, a_\mathrm{y})$ using a calibration function determined by sedimented or dried (in the case of $1.14\,\mu\mathrm{m}$ particles) particles with known z-position.

In order to define the ground truth for the particle detection and size classification, an outlier detection based on the Euclidean distance Z_err of the found particle images to the respective calibration curve in the $(a_\mathrm{x}, a_\mathrm{y})$ plane was used (Barnkob et al., 2021). For this, particles with Z_err below a global threshold of 7.5 pixel were initially considered as valid. In a second step, the acceptable Euclidean distance $Z_\mathrm{err,lim}(z')$ was adaptively determined as a function of the relative depth position z', leaving $90\,\%$ of the remaining particles declared as valid. However, if $Z_\mathrm{err,lim}(z')$ was locally

exceeding the arithmetic mean $\bar{Z}_{\mathrm{err,lim}}$ across all relative depth positions, $\bar{Z}_{\mathrm{err,lim}}$ was set as local threshold instead.

3. Methods

3.1. Size recognition based on particle image shape (PIS)

In order to implement a particle size recognition based on APTV measurements, two deterministic approaches are investigated. Within these two approaches, either the particle image intensity (see section 3.2) or the particle image shape (PIS) is used as the main discriminating feature. The latter is based on the link between the physical particle diameter d_p and the particle diameter in the image d_e, which is described by the following equation (Rossi et al., 2012):

$$d_e = M \left[d_p^2 + 1.49\lambda^2 \left(\frac{n_0^2}{NA^2} - 1 \right) + 4z'^2 \left(\frac{n_0^2}{NA^2} - 1 \right)^{-1} \right]^{1/2}. \tag{1}$$

Here, λ denotes the wavelength of the emitted light, n_0 the refractive index of the immersion medium of the lens, M the magnification and NA the numerical aperture of the lens. Besides the geometrical dependency, contributions of diffraction in the second term and of defocusing in the third term have to be considered as well. The impact of the geometric contribution on the particle image shape is evident from the deviating calibration functions for $2.47\,\mu\mathrm{m}$ and $5.03\,\mu\mathrm{m}$ polystyrene particles in the $(a_\mathrm{x}, a_\mathrm{y})$ plane in fig. 1. The valid particles cluster around the corresponding calibration function, while particles with an Euclidean distance $Z_{\mathrm{err}} > 0.75$ pixel from the calibration function are rejected for visualization. A classification of the particles according to their size can be realized based on the smaller Euclidean distance to the respective calibration function. For this, deviations in the particle image shape are required, which occur especially in the vicinity of the two focal planes z_1 and z_2 at minimum extension of the elliptical particle images in x- and y-direction, respectively. However, for strongly defocused particle images with extents of $a_x > 80$ pixel or $a_y > 100$ pixel, the defocus component predominates and the calibration functions take a similar course. For these regions, no reliable classification of the particles according to their size is feasible, which limits the applicable range of this approach to the vicinity of the focal planes.

3.2. Size recognition based on particle image intensity (PII)

In addition to the particle image shape, also the particle image intensity is influenced by the particle size (Hill et al., 2001) and thus allows a deterministic size recognition. However, the particle image intensity remains a complex quantity, which further depends on the fluorescence grade and dye, the intensity and duration of illumination, the sensitivity of the camera sensor, the optical system, the experimental setup and the spatial position of the particle. Since the experimental conditions and the measurement system remained unchanged in all experiments, associated systematic influences on the intensity of the particle images as well as random fluctuations in the
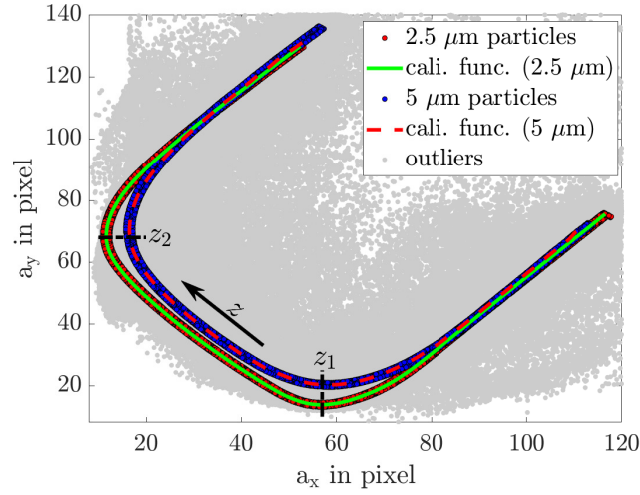
Figure 1. Valid $2.47\,\mu\text{m}$ (orange, $46.7\,\%$) and $5.03\,\mu\text{m}$ (blue, $54.8\,\%$) polystyrene particles with the corresponding calibration functions in the (a_x, a_y) plane. In this example, the particles were sedimented in a water filled chamber of PDMS, sealed by glas slides at the ceiling and bottom. Outliers with an Euclidean distance of $Z_{err} > 0.75$ pixel to the calibration function are depicted in gray. The positions of the two focal planes are marked as z_1 and z_2.

fluorescence grade of a particle species are neglected.

However, the spatial position of a particle $(x_\text{i}, y_\text{i}, z_\text{i})$ has a significant effect on the intensity of its particle image. Due to aberrations in the optical path and the laser light intensity profile, characteristic intensity distributions are formed in the xy-plane, as shown in fig. 2(a) for different particle species at a relative depth position $z_0' = 0\,\mu\text{m}$. When comparing the mean intensities at the center of the particle images as a function of the relative depth position in fig. 2(b), the stronger defocusing leads to a monotonically decreasing intensity as the distance from the focal planes (z_1, z_2) increases. To account for these influences, 2D regressions of the intensity profiles are approximated by second order polynomials in the xy-plane for each particle species at a constant depth position. For this, the approximations are based on APTV measurements of a laminar fluid flow using particles with a monomodal size distribution. The step size in z'-direction amounts to $\Delta z' = 1\,\mu\text{m}$. The size recognition for an unknown particle is performed according to the smallest absolute difference between its intensity and the value of the respective regression plane at position $(x_\text{i}, y_\text{i}, z_\text{i})$. An interpolated calibration function is used, since the size and thus the corresponding calibration function for the determination of the z'-coordinate in the multimodal particle mixture are initially unknown.

In order to determine the particle image intensity, the intensity values of all pixels within the ellipsoidal area of the particle image are summed up. This approach is more robust against random noise in the intensity level at individual pixel than taking the intensity value at the center of the particle image (Massing et al., 2016). Furthermore, not only the intensity peak but also the particle image size is considered, which proved to be beneficial for the size recognition in comparison to using e.g. the peak of a 2D Gaussian fit of the particle image intensity.
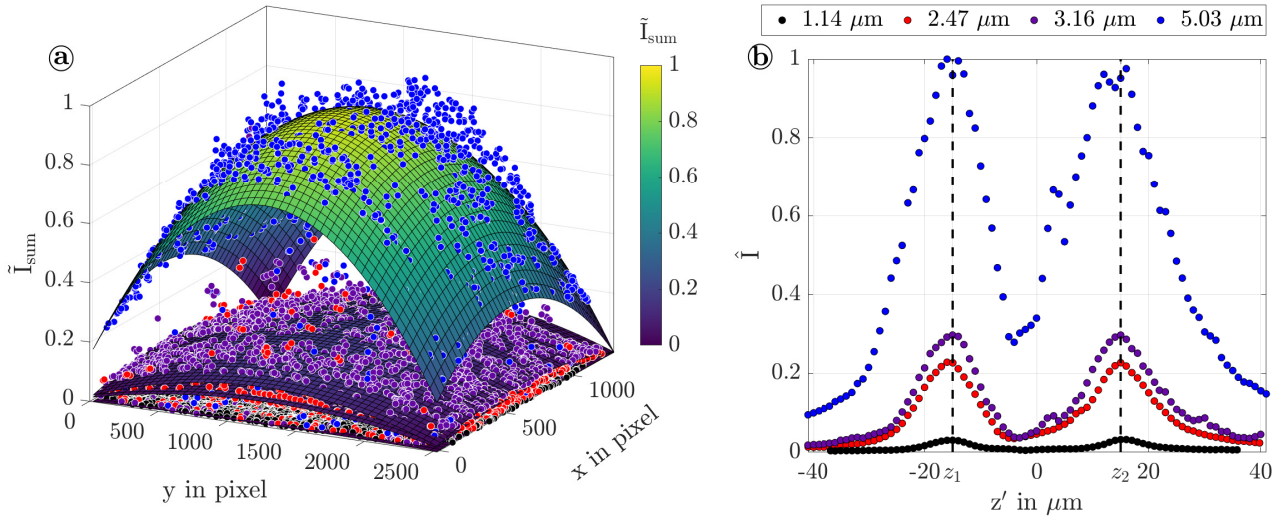
Figure 2. (a) Summed intensity from images of spherical polystyrene particles with various sizes along with regression planes at a relative depth position $z' = 0\,\mu\text{m}$. The intensity was normalized by the maximum intensity $I_{\text{sum,max}}$ of the $5.03\,\mu\text{m}$ particles to $\tilde{I}_{\text{sum}} = I_{\text{sum}}/I_{\text{sum,max}}$. (b) Mean normalized intensity peak at the center of the particle images as a function of the relative depth position z'. The positions of the focal planes are marked as z_1 and z_2. Please note that the legend in (b) applies to both plots. All data points are obtained from APTV measurement of a laminar channel flow.

3.3. Deep neural network (DNN)

The proposed particle size recognition is a typical classification task for which great progress has been made in recent years by applying deep neural networks (DNNs, Russakovsky et al. (2015)). These artificial networks use multiple layers of connected artificial neurons to detect image regions in which a desired object is suspected, extract associated features and assign the detected objects based on a given set of classes. The use of DNNs to detect the three-dimensional particle positions from raw images obtained in APTV measurements has been successfully demonstrated by König et al. (2020). Although the achievable accuracy in position determination remained lower compared to classical image processing algorithms for particle detection using monomodal particle solutions (Barnkob et al., 2021), the application of DNNs showed promising result when using bimodal particle mixtures (König et al., 2020).

The DNN used in this work combines the in-plane position determination of suspended particles with the classification of their size in multimodal particle solutions. For this, a network with a Faster R-CNN architecture (Ren et al., 2015) and a ResNet-50 as backbone for object detection is trained in Pytorch using the raw images from flow measurements with only one particle species in the microchannel. The learning rate of the pre-trained DNN is scheduled to linearly increase over one epoch to a value of 10^{-4} and successively decrease by a factor of 10 every epoch after the third epoch. The network is trained for 5 epochs with a batchsize of 16 and the AdamW optimizer (Loshchilov & Hutter, 2019) with a weight decay of 10^{-4} as regularization. Due to a large training set and short training duration, no data augmentation is used. The images are split into $80\,\%$ training, $10\,\%$ validation and $10\,\%$ test data. The images are rescaled to 8-bit as 16-bit images

significantly increase the training time and memory requirements of the network. High intensities are clipped to ensure that defocused particles of $1\,\mu\text{m}$ size are still resolved accurately. The different particle species are labeled as classes of objects according to their size. During the training process, regions which contain suspected particles are identified by bounding boxes enclosing the width and height of the particle images. The in-plane positions of the particles are determined based on the center of the bounding boxes. Correctly matched particles are required to have an Euclidean distance of less than 5 pixel to the corresponding label in the ground truth, which is based on the results of the classical APTV evaluation. Once the DNN has been trained on a NVIDIA A100 tensor-core GPU at the high-performance computing (HPC) cluster of TU Ilmenau, combinations of the acquisitions of bimodal particle flows serve to compare the size classification with the presented deterministic approaches during the inference.

4. Results and discussion

4.1. Size recognition in a bimodal particle mix

The performance of the proposed algorithms for particle size recognition is initially investigated on the basis of APTV measurements with particle solutions of bimodal size distribution. For this, spherical polystyrene particles with a diameter around $2.47\,\mu\text{m}$ are to be distinguished from $1.14\,\mu\text{m}$, $3.16\,\mu\text{m}$ or $5.03\,\mu\text{m}$ particles. Two examples of images acquired in a microchannel with a main flow from top to bottom are given in fig. 3(a,b) and fig. 3(c,d) for two different time instants. Using three separate inlets, the $2.47\,\mu\text{m}$ particles are pre-positioned on the left and $3.16\,\mu\text{m}$ particles on the right side of the microchannel to obtain the ground truth for size recognition (see section 2). Predictions of classified particles given by the deterministic algorithms are depicted in the upper half of each image, while particles suggested by the DNN are labeled in the bottom half. Particles correctly classified by the algorithms are declared as true positives (TP, green), incorrectly classified particles as false positives (FP, red), and non-detected particles are indicated as false negatives (FN, cyan), if they are considered as valid in the ground truth. Based on this sampling evaluation at two different time instants, a reliable classification by the DNN is evident, while there are several undetected or misclassified particles in the predictions of the deterministic algorithms.

To enable a quantitative comparison of the size recognition, the following metrics are determined.

$$\text{presicion} = \frac{TP}{TP + FP} \tag{2}$$

$$\text{recall} = \frac{TP_{\text{ref}}}{TP_{\text{ref}} + FN} \tag{3}$$

The precision serves as a measure for the quality of the classification and considers all predictions given by the respective algorithm. In contrast, the recall is based on the reference labels, which are validated with knowledge of the ground truth (see section 2), and quantifies the proportion of
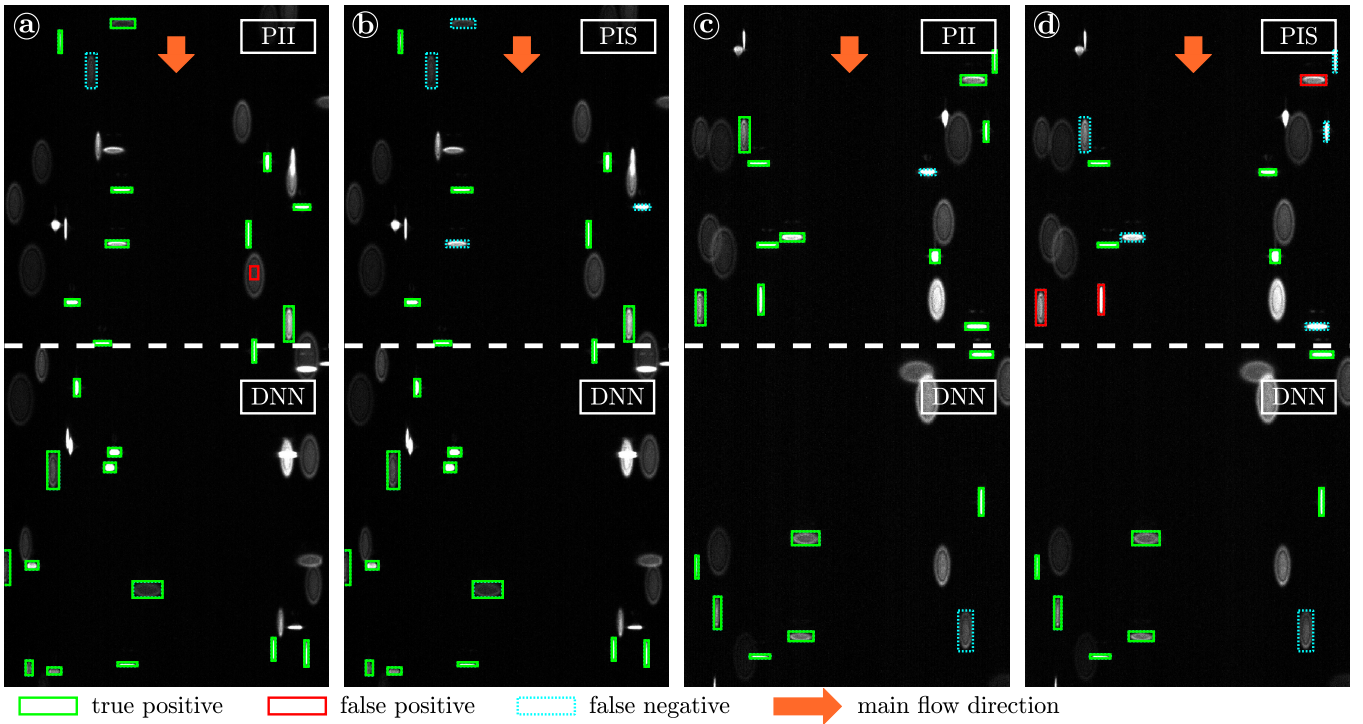
Figure 3. (a,c) Elliptically distorted particle images with labels given by the particle image intensity (PII) and the deep neural network (DNN) in the upper and lower half of the image, respectively. The classification based on the particle image shape (PIS) and the DNN is shown in (b,d). A different time instant is depicted in (c,d) compared to (a,b). Spherical $2.47\,\mu\mathrm{m}$ particles are located on the left side of the images, while $3.16\,\mu\mathrm{m}$ particles are on the right side.

particles that are correctly assigned (TP_{ref}) to the total number of valid particles. At this point it should be noted that the validation of the reference labels is based on the classical APTV evaluation and hence incorrect labels cannot be excluded entirely. Furthermore, strongly defocused or overlapping particle images are not considered in the reference labels.

In order to improve the performance of the algorithms, different outlier criteria are applied. Within the deterministic algorithms, the Euclidean distance Z_{err} to the respective calibration curve is used initially. In the size classification based on particle image intensity (PII), the distance to the nearest regression plane in the intensity level of the particles is further considered. The latter is investigated by the parameter err_{max} in the range of $[0.1, 1.1]\,\%$ of half the distance between the neighboring regression planes at the respective particle position ($x_{\mathrm{i}}, y_{\mathrm{i}}, z_{\mathrm{i}}$). Particle labels predicted by the DNN are validated by a threshold in the classification score, which is a measure of the confidence of the prediction.

In fig. 4, the achieved precision is plotted against the recall for the utilized algorithms under variation of the accepted threshold values in the outlier criteria. Depicted are results of the size recognition of a particle mixture of $2.47\,\mu\mathrm{m}$ and $5.03\,\mu\mathrm{m}$ polystyrene particles. For all algorithms employed, a characteristically increasing precision is revealed as the recall decreases. This trend is caused by a more rigorous validation, which leads to less particles being declared as valid and to a decrease in recall. Simultaneously, more reliable predictions are kept and the precision increases.
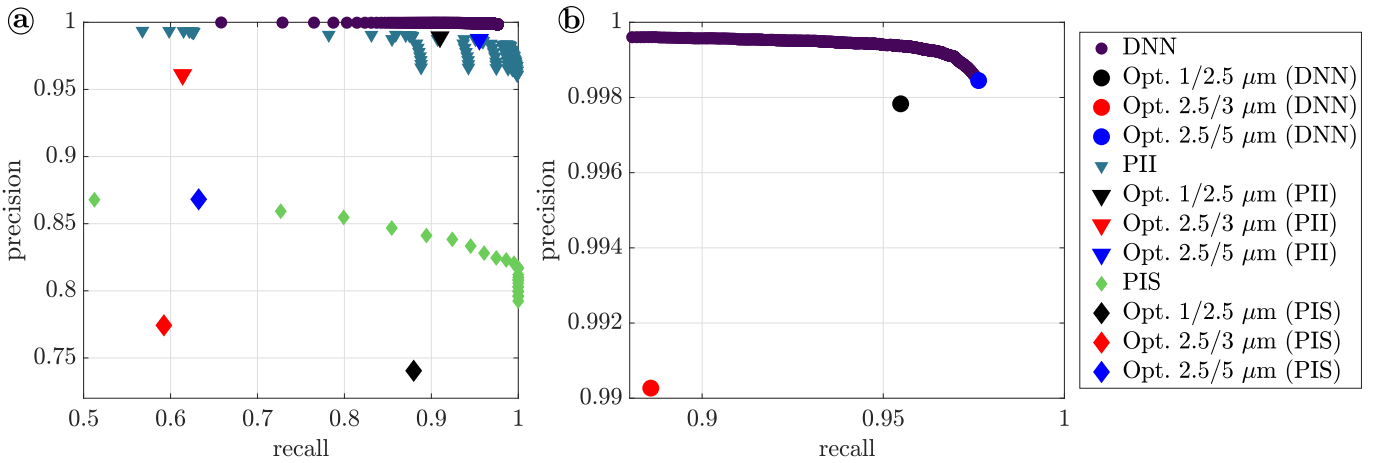
Figure 4. (a) Precision as a function of recall obtained for size recognition of $2.47\,\mu$m and $5.03\,\mu$m particles with DNN (dots), PII (triangle) and PIS (diamonds) under variation of the threshold in the outlier criteria. Optimized results are given for different combinations of the particle species. (b) Detailed representation of the results obtained by DNN.

To identify the best combination of thresholds in the outlier criteria within the grid search, the minimum of the weighted Euclidean distance $d = [(1-recall)^2 + \xi(1-precision)^2]^{\frac{1}{2}}$ to the optimal case with precision and recall equal one is calculated. In order to prioritize a reliable size classification higher than the yield, the precision is weighted by the coefficient $\xi = 100$.

The achievable precision following this optimization is plotted in fig. 4 for all combinations of particle species. Two trends emerge from the plot: First, both the recall and the precision for a given particle combination are consistently highest using the DNN and lowest using the PIS. Second, a distinction between $1.14\,\mu$m and $2.47\,\mu$m as well as $2.47\,\mu$m and $5.03\,\mu$m particles is more reliable than between $2.47\,\mu$m and $3.16\,\mu$m particles. This is caused by less distinctive features regarding the shape or intensity of the particle images corresponding to the latter combination of particle sizes. An exception is the distinction between $1.14\,\mu$m and $2.47\,\mu$m particles on the basis of PIS. In this case, deviations in the calibration functions of the two particle species turn out to be the smallest, which results in an inefficient outlier detection by Z_{err} and a lower precision. By using the PII and the DNN, a precision above $96\,\%$ is reached consistently. Greater limitations exist with regard to the recall for size detection according to PII, while values above $88\,\%$ were always attained with the DNN.

After optimizing the algorithms with respect to particle size recognition, the achievable precision and recall as a function of the relative depth position z' are evaluated based on fig. 5. Using PIS for size classification, the highest precision can be achieved near the focal planes (z_1, z_2), while it decreases with increasing distance to z_1 and z_2. This is due to the course of the calibration functions, which show the largest difference especially in these areas (see section 2). Furthermore, the highest recall can also be achieved in the vicinity of the focal planes, since the extent of the particle images found scatters closely around the associated calibration function and only a few particles are rejected. Due to the smallest distance between the calibration functions, the outlier detection becomes ineffective when distinguishing between $1.14\,\mu$m and $2.47\,\mu$m particles, which
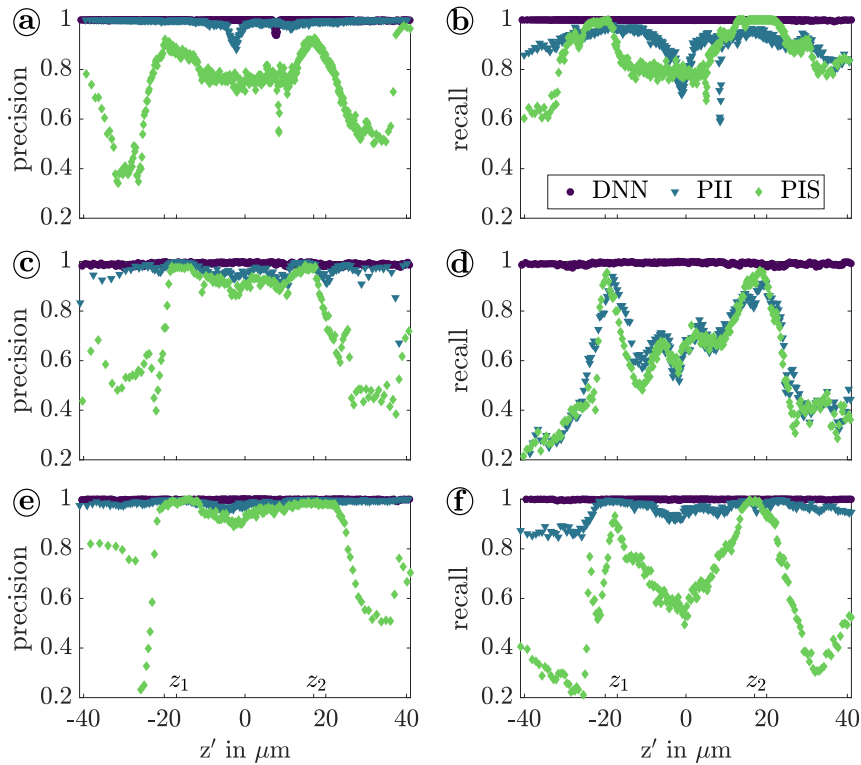
Figure 5. Precision and recall as a function of the relative depth position z' for size classification of bimodal particle solutions of sizes $1.14\,\mu\mathrm{m}$ and $2.47\,\mu\mathrm{m}$ (a,b), $2.47\,\mu\mathrm{m}$ and $3.16\,\mu\mathrm{m}$ (c,d), as well as $2.47\,\mu\mathrm{m}$ and $5.03\,\mu\mathrm{m}$ (e,f). Please note that the legend in (b) applies to all subfigures.

leads to the lowest precision in this comparison (see fig. 5(a) and (b)).

In contrast, a significantly more uniform precision with higher values is obtained across z' when the PII is considered. This demonstrates a robust size detection by this algorithm also for strongly defocused particle images. The influence of the two outlier criteria is evident in the recall. When distinguishing between $1.14\,\mu\mathrm{m}$ and $2.47\,\mu\mathrm{m}$ as well as $2.47\,\mu\mathrm{m}$ and $5.03\,\mu\mathrm{m}$ particles, a more rigorous validation with respect to err_{max} leads to an almost uniform recall over z'. However, since the difference in intensity between the $2.47\,\mu\mathrm{m}$ and $3.16\,\mu\mathrm{m}$ particles is lower, a more rigorous validation with respect to Z_{err} was chosen, which results in a recall that is closer to that obtained by PIS.

The best results in the size classification of bimodal particle solutions are obtained using the DNN. Both precision and recall are subject to very small variations across the relative depth position z' with values above $99\,\%$ in $89.66\,\%$ and $90.95\,\%$ of the data, respectively. Thus, only 1668 of the $1\,273\,379$ predicted particles are incorrectly classified in total using the DNN.

4.2. Particle size recognition of multiple classes

After applying and optimizing the particle size recognition on images of bimodal particle solutions, multi-class problems are analyzed in the following. For this, combinations of the APTV

measurements with two different particle species are used. The outlier criteria optimized in section 4.1 are adaptively applied within the deterministic algorithms depending on the predicted particle class. For size recognition by the DNN, the outlier detection is performed using a constant threshold in the classification score, which is optimized for each combination of particle species according to the minimum of the criterion d (see section 4.1).
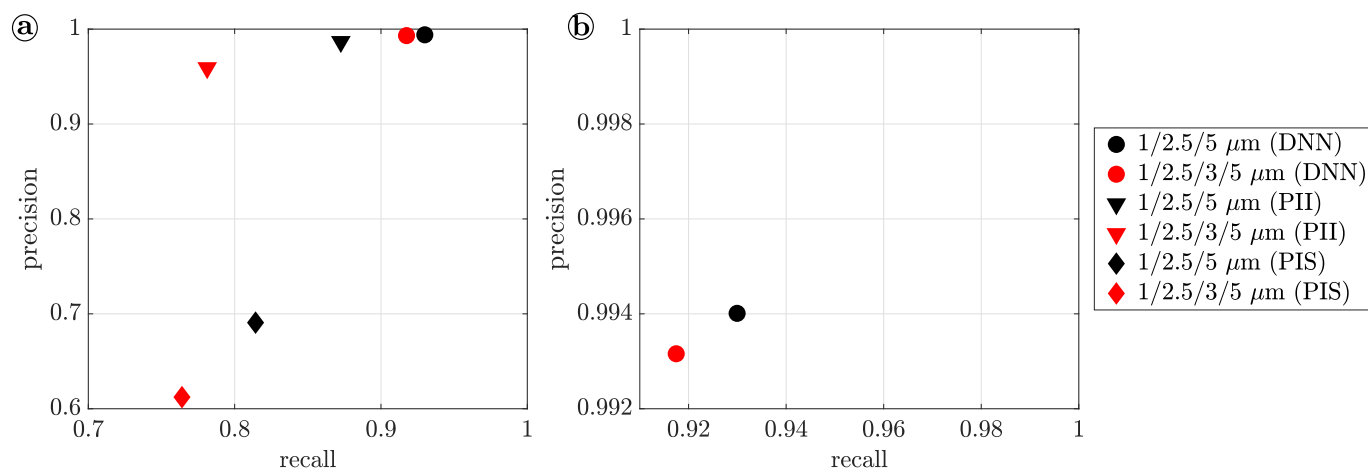

Figure 6. (a) Precision as a function of recall obtained in multi-class classification by using DNN (dots), PII (triangles) and PIS (diamonds). (b) Enlarged view of the results obtained with DNN.

The achieved precision in particle size recognition is shown in fig. 6 for the proposed algorithms as a function of recall. The classification of spherical polystyrene particles with $1.14\,\mu m$, $2.47\,\mu m$ and $5.03\,\mu m$ as well as $1.14\,\mu m$, $2.47\,\mu m$, $3.16\,\mu m$ and $5.03\,\mu m$ in diameter are investigated. With the extension to three and four classes of particles, the precision does not significantly decrease with values above 0.95 using PII and DNN, which still perform considerably better than PIS. With regard to the deterministic algorithms PIS and PII, the achievable precision and recall for the classification of three particle species are consistently above the results of the four class discrimination. This trend is expected to persist for an increasing number of classes within the same size range. Furthermore, only a marginal decrease in precision for PII in the three-class problem is revealed compared to the distinction between two of the involved particle species. The reason for this is found in the deviation between the regression planes in the intensity level of the different particles, which turns out to be comparably large and facilitates a size classification. In the case of a classification with all particle sizes, the precision decreases by approx. $3\,\%$ and the recall by about $12\,\%$ compared to the discrimination of $1.14\,\mu m$, $2.47\,\mu m$ and $5.03\,\mu m$ sized particles.

For the classification according to the PIS, deviations between the calibration functions are crucial, which are the smallest for the discrimination of $1.14\,\mu m$ and $2.47\,\mu m$. These particle species are included in the three-class classification, whereby the precision already drops to approx. $69\,\%$. Simultaneously, the recall of approx. $81\,\%$ indicates that the outlier detection according to Z_{err} is rather inaccurate, which might lead to the low precision. However, when the DNN is used for size classification, the achieved precision still clusters around $99.3\,\%$ in both cases.
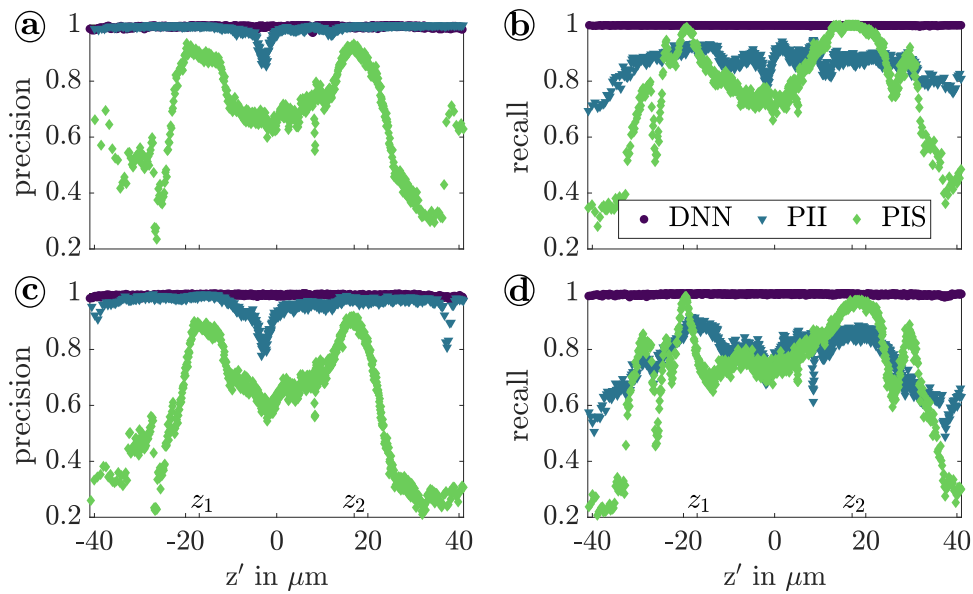
Figure 7. Precision and recall as a function of the relative depth position z' for the classification of $1.14\,\mu\text{m}$, $2.47\,\mu\text{m}$ and $5.03\,\mu\text{m}$ (a,b) as well as $1.14\,\mu\text{m}$, $2.47\,\mu\text{m}$, $3.16\,\mu\text{m}$ and $5.03\,\mu\text{m}$ sized particles (c,d) by DNN, PII and PIS.

When comparing the precision and recall over the relative depth position as shown in fig. 7, the results obtained in the multi-class problems are somewhat similar to those obtained in the two-class problems. Using the DNN yields a very uniform profile of recall with values larger than $97.6\,\%$, while a high recall for PIS is achieved only in the vicinity of the focal planes z_1 and z_2. In the context of size classification into four classes, the recall obtained by PII converges to the results with PIS, however the contribution of strongly defocused particles with $|z'| > 30\,\mu\text{m}$ to the outliers increases. This is due to the more rigorous validation according to Z_{err} for the distinction of $2.47\,\mu\text{m}$ and $3.16\,\mu\text{m}$ sized particles.

With regard to precision, a local drop of precision is evident between the two focal planes when using PII, which is already visible when classifying $1.14\,\mu\text{m}$ and $2.47\,\mu\text{m}$ particles in fig. 5(a). In this region, predicted particles are assigned to a too low intensity, which causes them to be declared primarily as $1.14\,\mu\text{m}$ sized particles. This might originate from unrejected fragments of strongly defocused particle images, as seen in fig. 3(a). These fragments have a very low intensity, but cannot be rejected during validation by the utilized outlier criteria.

As illustrated in fig. 8(a), the number of valid particle images varies for different particle sizes. The smaller the particles, the higher the chosen seeding density, which means that large particles are underrepresented in the data sets. This underrepresentation of $5.03\,\mu\text{m}$ particles in the training data is reflected in the highest proportion of misclassifications by the DNN. An exception to this trend is the proportion of $2.47\,\mu\text{m}$ particles of about $49\,\%$ of the total number of valid particles, since these occur in every bimodal particle mix. Concurrently, the largest fraction of particle images misclassified by deterministic approaches is due to $2.47\,\mu\text{m}$ particles. For detailed evaluation, fig. 8(b) lists the relative frequencies of the particle sizes to which the $2.47\,\mu\text{m}$ particles are misclassified. While these are declared as $3.16\,\mu\text{m}$ sized particles to about $97.8\,\%$ by the DNN, it is more likely
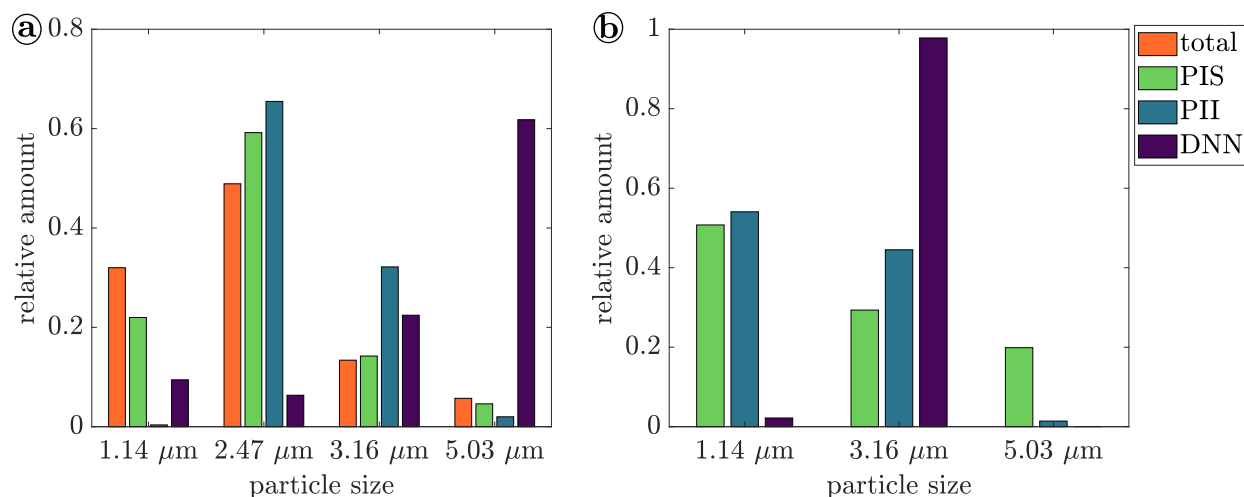
Figure 8. (a) Relative distribution of the number of valid particles (total) and relative frequency of incorrectly classified particles by the proposed algorithms (PIS, PII, DNN) versus particle size. (b) Relative frequency of particle sizes to which $2.47\,\mu m$ particles were misclassified.

that the false predictions based on the deterministic algorithms classify their diameter as $1.14\,\mu m$. This result further supports the hypothesis of incorrectly detected fragments of defocused particle images.

In summary, the applicability of the proposed algorithms to multi-class recognition is successfully demonstrated. Similar to the results obtained in the distinction of particle images of bimodal particle solutions, the highest precision and recall is achieved using the DNN. The DNN performs very stable over the whole range of relative depth positions and does not imply any limitations regarding the defocusing of the particle images in the observed range.

5. Conclusion

In this study, the particle size recognition of tracer particle solutions with bimodal size distribution is investigated based on APTV measurements in a microchannel. By applying deterministic algorithms that utilize the particle image shape (PIS) or particle image intensity (PII), a discrimination of spherical $2.47\,\mu m$ and $3.16\,\mu m$ sized particles is achieved with a precision of up to $96\,\%$. The results are compared with the performance of a deep neural network (DNN) trained for object detection and particle size classification. The examined DNN consistently achieve a precision higher than $99\,\%$ in the bimodal particle solutions studied, which further permits its use even for strongly defocused particle images. Once various outlier criteria are optimized based on the discrimination of images of bimodal particle mixtures, the application to multi-class classification is performed. Fluorescent polystyrene particles in the range of $1.14\,\mu m$ to $5.03\,\mu m$ are distinguished into four classes with a precision of up to $99.3\,\%$, while a recall of $91.7\,\%$ is maintained. The obtained results demonstrate the capability of a reliable particle size recognition using a standard APTV setup for microfluidics. The introduced algorithms allow a low cost extension of APTV to

particle solutions with multimodal size distribution, which does not require any adaptation of the existing measurement equipment or the use of different fluorescent dyes for each particle species. Furthermore, the training of the DNN is based on flow measurements, which can be integrated into the measurement procedure with reasonable effort and do not require rather time consuming measurements of sedimented particles as usual.

Acknowledgements

References

Barnkob, R., Cierpka, C., Chen, M., Sachs, S., Mäder, P., & Rossi, M. (2021). Defocus particle tracking: a comparison of methods based on model functions, cross-correlation, and neural networks. *Measurement Science and Technology*, *32*(9), 094011.

Cierpka, C., Rossi, M., Segura, R., & Kähler, C. J. (2011). On the calibration of astigmatism particle tracking velocimetry for microflows. *Measurement Science and Technology*, *22*(1), 015401.

Cierpka, C., Rossi, M., Segura, R., Mastrangelo, F., & Kähler, C. J. (2012). A comparative analysis of the uncertainty of astigmatism-µPTV, stereo-µPIV, and µPIV. *Experiments in Fluids*, *52*(3), 605–615.

Cierpka, C., Segura, R., Hain, R., & Kähler, C. J. (2010). A simple single camera 3C3D velocity measurement technique without errors due to depth of correlation and spatial averaging for microfluidics. *Measurement Science and Technology*, *21*(4), 045401.

Hill, S. C., Pinnick, R. G., Niles, S., Fell, N. F., Pan, Y.-L., Bottiger, J., Bronk, B. V., … Chang, R. K. (2001). Fluorescence from airborne microparticles: dependence on size, concentration of fluorophores, and illumination intensity. *Applied Optics*(40), 3005–3013.

König, J., Chen, M., Rösing, W., Boho, D., Mäder, P., & Cierpka, C. (2020). On the use of a cascaded convolutional neural network for three-dimensional flow measurements using astigmatic PTV. *Measurement Science and Technology*, *31*(7), 074015.

Loshchilov, I., & Hutter, F. (2019, 11). Decoupled weight decay regularization. In *International conference on learning representations*.

Massing, J., Kaden, D., Kähler, C. J., & Cierpka, C. (2016). Luminescent two-color tracer particles for simultaneous velocity and temperature measurements in microfluidics. *Measurement Science and Technology*, *27*, 115301.

Ren, S., He, K., Girshick, R., & Sun, J. (2015). Faster R-CNN: Towards real-time object detection with region proposal networks. In *Proceedings of the 28th international conference on neural information processing systems - Volume 1* (p. 91–99). Cambridge, MA, USA: MIT Press.

Rossi, M., Segura, R., Cierpka, C., & Kähler, C. J. (2012). On the effect of particle image intensity and image preprocessing on the depth of correlation in micro-PIV. *Experiments in Fluids*, *52*(4), 1063–1075.

Russakovsky, O., Deng, J., Su, H., Krause, J., Satheesh, S., Ma, S., ... Fei-Fei, L. (2015). ImageNet Large Scale Visual Recognition Challenge. *International Journal of Computer Vision (IJCV)*, *115*(3), 211-252.

Sachs, S., Baloochi, M., Cierpka, C., & König, J. (2022). On the acoustically induced fluid flow in particle separation systems employing standing surface acoustic waves - Part I. *Lab on a chip*, *22*, 2011–2027.

Sajeesh, P., & Sen, A. K. (2014). Particle separation and sorting in microfluidic devices: a review. *Microfluidics and Nanofluidics*, *17*(1), 1–52.

Wu, M., Ozcelik, A., Rufo, J., Wang, Z., Fang, R., & Jun Huang, T. (2019). Acoustofluidic separation of cells and particles. *Microsystems & nanoengineering*, *5*, 32.